

Non-volatile Multistate Magnetic Switching via Spin-orbit Torque and Intrinsic Anisotropy

Fei Ye^{1,†}, Chunzheng Wang^{2,†}, Xue Zhang^{3,†}, Sihai Jiao^{2,†}, Zhongjie Wang^{2,*}, Long Cheng¹,
Zhifeng Zhu^{3,*}, Chunlei Gao² & Xiaofang Zhai^{1,4,*}

¹ School of Physical Science and Technology, ShanghaiTech University, Shanghai 201210, China

² State Key Laboratory of Surface Physics, Institute for Nanoelectronic Devices and Quantum Computing, and Department of Physics, Fudan University, Shanghai 200438, China

³ School of Information Science and Technology, ShanghaiTech University, Shanghai 201210, China

⁴ State Key Laboratory of Quantum Functional Materials, School of Physical Science and Technology, ShanghaiTech University, Shanghai 201210, China

[†] Equally contributed to this work.

* Corresponding authors.

* E-mails:

zhaixf@shanghaitech.edu.cn; zhongjiewang18@fudan.edu.cn; zhuzhf@shanghaitech.edu.cn

ABSTRACT

While current-induced bistate spin-orbit torque (SOT) switching has been well established, deterministic electrical control of multiple magnetic states remains a central challenge in spintronics. Here, we realize a conceptually new multistate SOT device in a SrIrO₃/SrRuO₃ bilayer, hosting four intrinsically stable yet electrically distinguishable magnetic states, including two in-plane canted (IP_c[±]) and two out-of-plane canted (OP_c[±]) states. Pulsed current excitations fully map all twelve deterministic transitions among the four states, establishing a robust switching protocol defined by two characteristic current densities. In-situ scanning nitrogen-vacancy (NV) center magnetometry provides direct real-space evidence for the previously unobserved IP_c[±] states, and spin dynamics simulations uncover a two-step switching pathway, driven by the concerted action of spin torques and the effective anisotropy field within the fourfold anisotropy landscape. Our demonstration of the intrinsic multistate SOT device directly addresses the density bottleneck of conventional bistate SOT technology, establishing a powerful paradigm for compact, high-speed, and energy-efficient multistate spintronics.

Keywords: all-oxide spintronics, spin-orbit torque, multistate memory, in-situ NV center magnetometry

INTRODUCTION

SOT devices that enable nonvolatile magnetization switching via spin current injection are central to next-generation, high speed and energy-efficient spintronics. A typical SOT structure consists of a heavy metal (HM) layer adjacent to a ferromagnetic (FM) layer. When a charge current flows through the HM layer along the x direction, the spin-Hall effect generates a pure spin current with polarization $\vec{\sigma}$ along the y direction, which is injected into the FM layer [1-3]. The spin current exerts field-like (FL) torque $\vec{\tau}_{\text{FL}} \sim \vec{m} \times \vec{\sigma}$ and damping-like (DL) torque $\vec{\tau}_{\text{DL}} \sim \vec{m} \times (\vec{\sigma} \times \vec{m})$ on the magnetization \vec{m} , driving switching dynamics well described by the Landau-Lifshitz-Gilbert (LLG) model [4]. To date, bistable switching between two antiparallel states has advanced significantly, including demonstrations of field-free switching [5-8] and the use of materials with large spin-Hall angles (θ_{SH}) to minimize switching power [9,10]. However, the key bottleneck preventing SOT technology from realizing its full potential for broad applications is the low storage density imposed by its multi-terminal read/write design. Recently, increasing attention has turned to multistate SOT switching, which aims to overcome the fundamental capacity limits of binary systems and open new avenues for multistate spintronic devices.

Multistate SOT devices have so far been primarily realized by stacking multiple FM layers, each capable of being excited into different magnetic states to produce a composite multi-level response [11-13]. While this approach achieves high storage density, it comes at the cost of increased fabrication complexity and expense. A fundamentally different strategy remains unexplored: the realization of intrinsic multistate SOT devices, engineered from the ground up for superior scalability and reliability. Achieving this requires overcoming two key challenges. First, suitable FM materials must be identified that exhibit intrinsic multiaxial magnetic anisotropy (MA), in which multiple magnetic states can be distinctly addressed electrically. Second, strategic design of the SOT device is needed to enable controlled transition between these energetically stable states. The complex oxide SrRuO₃ (SRO) is particularly appealing as it features highly tunable MA, including perpendicular [14], canted [15], and even eight-fold [16] MAs, arising from the interplay among $4d$ electron correlation, strong spin-orbital coupling and lattice distortion. Moreover, bistate SOT devices employing SRO and SrIrO₃ (SIO) heterostructures, where SIO exhibits an intrinsically high θ_{SH} (~ 0.5) [17], have already been demonstrated with high charge to spin conversion efficiencies [7,18]. These features make the SIO/SRO heterostructure an excellent platform for developing intrinsic multistate SOT devices.

In this work, we demonstrate an intrinsic multistate SOT device based on a SIO/SRO bilayer epitaxially grown on (0 0 1) SrTiO₃. The SRO layer hosts four electrically readable canted states (IP_c^\pm , OP_c^\pm), which can be deterministically and non-volatilely switched via two distinct current thresholds: $|J| \geq J_{c1}$ for toggling between IP_c^\pm states, and $|J| = J_{c2}$ for driving transitions from IP_c^\pm to OP_c^\mp . Remarkably, the device exhibits minimum detected thresholds $J_{c1} = 6.7 \times 10^6$ A/cm² and $J_{c2} = 4.4 \times 10^6$ A/cm², comparable to those of state-of-the-art bistate SOT devices. Scanning NV-center microscopy visualizes the previously unobserved IP_c^\pm states and demonstrates their in-plane magnetization switching. Spin dynamics simulations reveal that the cooperative action of τ_{DL} , τ_{FL} and the effective anisotropy field H_{eff} drives a two-step switching pathway via an intermediate state within the four-fold anisotropy landscape. By mapping all twelve transition pathways, eight via single-pulse excitations and four via double-pulse excitations, we establish a robust and precise four-state read/write protocol. This study defines a new paradigm for compact, high-density SOT devices, breaking through the intrinsic storage constraint of conventional bistate architectures. The established design principle is readily applicable to multiaxial spin-canted material families.

RESULTS

The Four-state SOT Switching Loops and Two Critical Current Thresholds

Figure 1a, b presents the schematic of the SIO/SRO bilayer lattice, the Hall-bar device geometry and representative SOT switching examples ($OP_c^+ \rightarrow IP_c^+$ and $IP_c^+ \rightarrow OP_c^-$). Here, the ‘+/-’ signs denote positive/negative IP or OP magnetization directions, and the subscript ‘c’ indicates canting. Details of device fabrication, structural characterization, magneto-transport and magnetization measurements are provided in the Experimental Section and Fig. S1-4.

Figure 1c presents representative SOT switching loops measured at 60 K under external magnetic fields of $H_x = 0, 100, 300$ and 1000 Oe. Unlike conventional bistate devices, four distinct anomalous Hall resistance (R_H) plateaus are observed in all switching loops: the top (OP_c^+) and bottom (OP_c^-) plateaus appear at small $|J|$, while the left (IP_c^-) and right (IP_c^+) plateaus arise at large $|J|$, as exemplified by the 300 Oe loop in Fig. 1c. Between these plateaus, R_H exhibits clear transitions: from OP_c^\pm to IP_c^\pm when $|J|$ exceeds J_{c1} , and from IP_c^\pm to OP_c^\mp when $|J|$ decreases to J_{c2} . Similar plateau structures and transition behaviors are also observed in loops measured under negative H_x (Fig. S5). Figure 1d summarizes the dependence of J_{c1} and J_{c2} on H_x , both decreasing with the increasing field when $H_x \leq 100$ Oe. But they behave differently when $H_x > 100$ Oe: J_{c1} continuously decreases with increasing H_x reaching 7.3×10^6 A/cm² when $H_x = 1000$ Oe, while J_{c2} remains constant at 5.5×10^6 A/cm². The distinct field

dependences of J_{c1} and J_{c2} indicate that the two types of switching processes are governed by different underlying mechanisms.

We further investigate the temperature dependence of the four-state SOT switching. **Figure S6** shows the switching loops measured between 2 K and 80 K under a constant $H_x = 1000$ Oe, which consistently exhibit robust four-state switching behaviors. The extracted J_{c1} and J_{c2} are shown in **Fig. 1e**, which progressively decrease with increasing temperature, likely due to the reduction in saturation magnetization at elevated temperatures [19]. As T increases from 2 K to 80 K, J_{c1} and J_{c2} decrease by about 35%, reaching minima of 6.7×10^6 A/cm² and 4.4×10^6 A/cm², respectively. The corresponding power dissipations are estimated using $P_{sw} = \rho_{xx} J_c^2$, where ρ_{xx} is the longitudinal resistivity, yielding $P_{sw1} = 1.03 \times 10^{16}$ W/m³ and $P_{sw2} = 4.6 \times 10^{15}$ W/m³. We further benchmark these $P_{sw1,2}$ values, together with the reported spin-Hall angle of SIO ($\theta_{SH} \sim 0.5$) [17], against state-of-the-art bistate SOT devices across various material platforms. As summarized in **Fig. 1f**, even in its prototype form, the intrinsic four-state SOT device already achieves energy efficiencies comparable to, or even surpassing, those of many advanced bistate devices [1,2,7,20-30], suggesting considerable potential for future optimization.

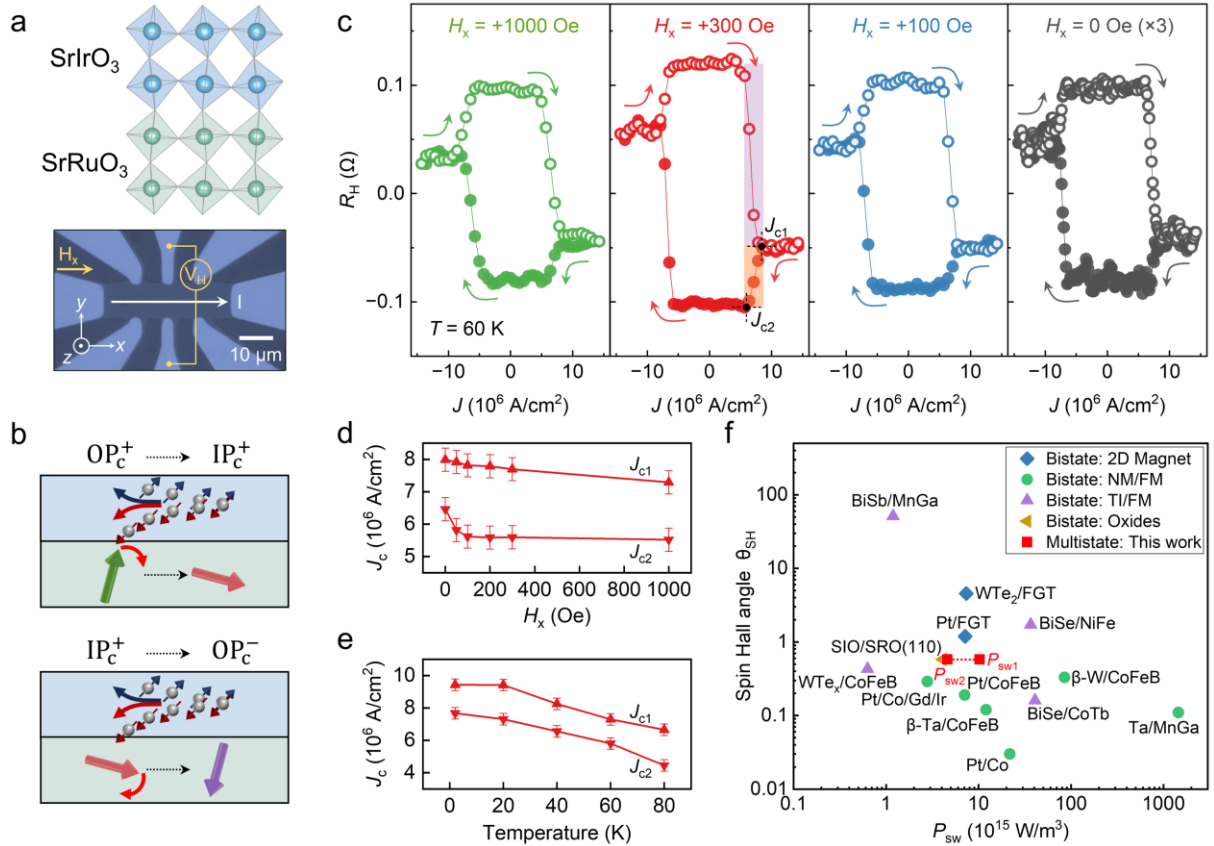


Figure 1. Current-induced magnetization switching in a four-state SOT device. (a) Schematic illustration of the bilayer structure and optical image of the Hall-bar device and measurement

schematics. (b) Cartoons of the spin current generation and switching of the FM moment from OP_c^+ to IP_c^+ and from IP_c^+ to the OP_c^- . (c) Magnetization switching loops at 60 K. Arrows indicate the current sweeping directions. (d) The critical current densities of J_{c1} and J_{c2} as functions of in-plane field H_x at 60 K, and (e) as functions of temperature with fixed $H_x = 1000$ Oe. (f) Spin-Hall angle θ_{SH} and the switching power P_{sw} of advanced bistate SOT devices [1, 2, 7, 20-30] and the current four-state device (data taken at 80 K). The two red points denote the P_{sw1} (right) and P_{sw2} (left), respectively.

In-situ NV-center Magnetometry Imaging and Static-state Torque Analysis

In typical ferroic systems, polarization or magnetization switching is coercive, requiring an external stimulus large enough to overcome an energy barrier, while sub-threshold excitations fail to induce switching. However, the switching process from IP_c^\pm to OP_c^\mp in our device is ‘abnormal’: starting from IP_c^\pm , larger pulsed-current with $|J| \geq J_{c1}$ preserve the initial state, whereas smaller excitation with $|J| = J_{c2}$ triggers the switching to OP_c^\mp . This unusual behavior implies a complex interplay between current-induced spin torques and the multiaxial energy landscape. To uncover the underlying mechanism, we perform real-space imaging of the four magnetic states using in-situ scanning NV-center magnetometry.

The in-situ measurement setup and the single spin direction of the NV-center (NV axis) are schematically illustrated in Fig. 2a, b. The NV-axis resides in the yz plane, tilted 54.7° from the z -axis. Current pulses and an external field of 300 Oe are applied along the x -axis immediately before NV measurements. More measurement details are provided in the Experimental Section. Micrometer-scale domain structures corresponding to the four states are shown in Fig. 2d, f, h, and j, with their positions indicated by dots in Fig. 2g. The application of current pulses rearranges the domain configuration, leading to disparate magnetic textures. Notably, a sharp contrast is observed between maps of the IP_c^+ and IP_c^- states, obtained after +20 mA and -20 mA pulses, respectively. In these magnetic textures, most regions exhibit a clear reversal of the stray field (indicated by guidelines in Fig. 2f and 2h), showing that the domain configuration is preserved while the magnetization within each domain is inverted. This implies that domains in the IP_c^\pm states can be collectively reversed. In contrast, the OP_c^\pm states exhibit stochastic rearrangements of both domain configuration and polarization, rather than a uniform reversal. It should be noted that the NV axis is more aligned with the IP_c^\pm magnetization than the OP_c^\pm state, as schematically shown in Fig. 2b, which limits the projection of the latter onto the detection axis and may hinder clear visualization. The strong

contrast observed between the IP_C^\pm maps implies a substantial projection of their magnetization along the NV axis (y -direction), agreeing to SQUID measurements shown in Fig. S3.

Figure 2c, e, i, k shows the orientations and relative magnitudes of the torque components acting on the four initial states, corresponding respectively to Fig. 2f, d, h, and j. The damping-like torque τ_{DL} consistently drives the magnetization \vec{m} towards the spin polarization direction ($\pm\hat{y}$). It indicates that τ_{DL} is responsible for the switching from OP_C^\pm to IP_C^\pm , assisted by the external field torque τ_{ext} , as shown in Fig. 2e and 2i. In comparison, the field-like torque τ_{FL} and τ_{ext} are precessional in nature, with dynamically evolving directions which may exert a more stochastic influence on the magnetization. In the IP_C^\pm states (Fig. 2c and 2k), τ_{FL} and τ_{ext} approximately act in the same direction when $m_x > 0$, but oppose each other when $m_x < 0$. When the current amplitude falls below a critical threshold, the magnitude of τ_{DL} declines, rendering it insufficient to maintain alignment along the IP_C^\pm easy axis. Under these conditions, the combined effects of τ_{FL} and τ_{ext} may drive the precessional motion of \vec{m} away from the IP_C^\pm easy axis, eventually allowing relaxation into the OP_C^\pm states.

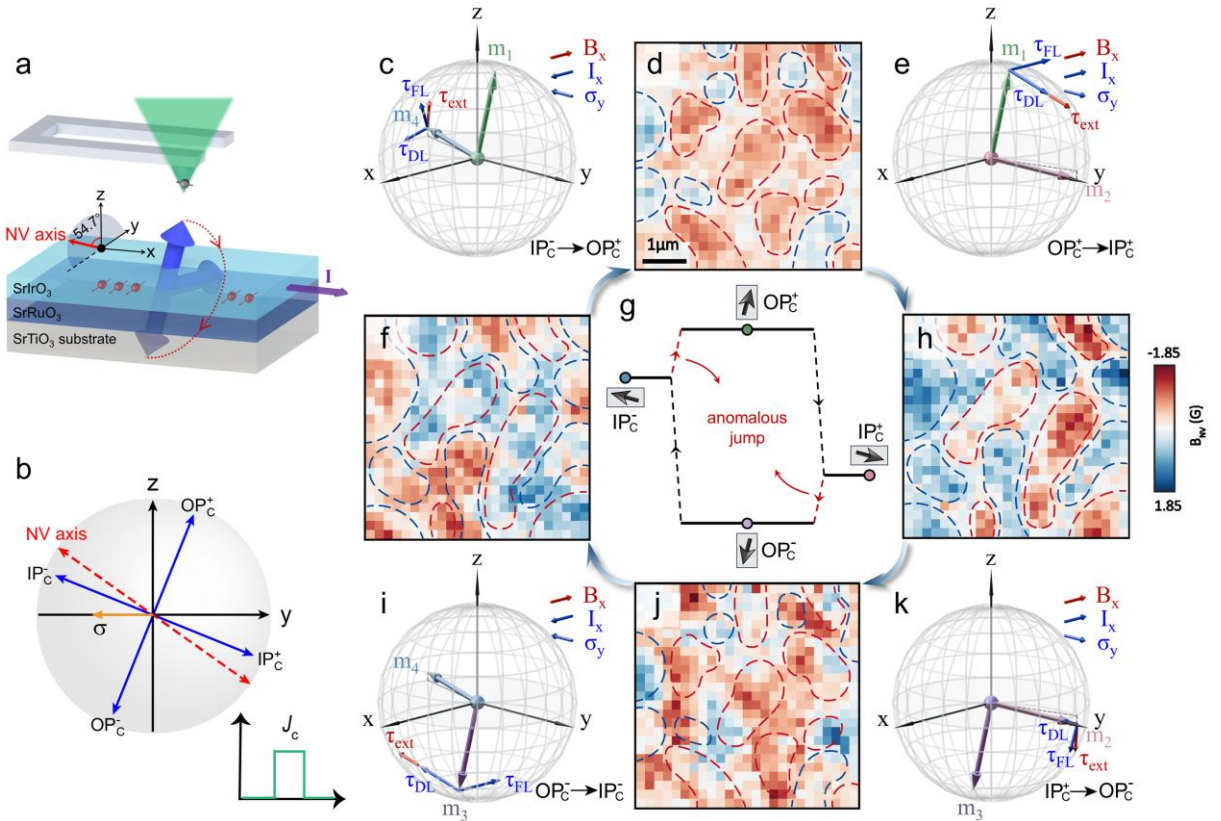


Figure 2. In-situ NV-center magnetometry imaging and static-state torque analysis. (a) Schematic of the scanning NV-center magnetometer. The variation of the magnetization (blue arrow) in SRO can be detected by the NV-center through changes in the magnetic field. (b) Configurations of relative orientations between the NV-axis and magnetizations. (c), (e), (i),

and (k) depict the four-state magnetization switching process governed by multiple torques. (g) Sketch of the four-state switching loop, where the IP_c^\pm to OP_c^\pm transition is coined as ‘anomalous’ jump (red arrows). (d), (f), (h), and (j) present magnetic textures corresponding to OP_c^+ , IP_c^- , IP_c^+ , OP_c^- revealed by NV-center respectively, where the red and blue dashed lines delineate the contours of the corresponding magnetic domains.

Spin Dynamics Simulations of the Four-state Switching

To fully understand the experimental observations and validate the above proposed mechanism, we perform the spin dynamics simulations [31] by solving the Landau-Lifshitz-Gilbert-Slonczewski (LLGS) equation: $\frac{\partial \vec{m}}{\partial t} = -\gamma \vec{m} \times (\vec{H}_{\text{eff}} + \vec{H}_x) + \alpha \vec{m} \times \frac{\partial \vec{m}}{\partial t} - \gamma B_D \vec{m} \times (\vec{m} \times \vec{\sigma}) + \gamma B_F \vec{m} \times \vec{\sigma}$. The four terms on the right-hand side represent precession, Gilbert damping, DL torque and FL torque, respectively. Here, γ is the gyromagnetic ratio and the effective field is $\vec{H}_{\text{eff}} = -\frac{\partial \mathcal{H}}{\partial \vec{m}}$. B_D and B_F denote the magnitudes of the DL and FL torques, respectively. The Hamiltonian is $\mathcal{H} = K_u \sin^2 \theta - K_y \sin^2 \theta \sin^2 \varphi - K_x \sin^2 \theta \cos^2 \varphi - K_{4u} \cos(4\theta)$, where K_u , K_y and K_x are the uniaxial anisotropy constants along the z , y , and x axes, and K_{4u} represents the fourfold anisotropy energy,[32] indispensable for the four-state switching. θ and φ are the polar and azimuthal angles in the spherical coordinate. In accordance with the experiment setup, a current J along $+\vec{x}$ induces spin polarization $\vec{\sigma}$ along $-\vec{y}$. Magnitudes of B_D , K_u , K_y and K_x are based on experiments, while $B_F = \beta B_D$ is optimized to reproduce the four-state switching loop in Fig. 3b, consistent to the experiment. More parameter optimization details are provided in methods section and Fig. S7. The energy diagram in Fig. 3a derived from the Hamiltonian reveals the four ground states corresponding to OP_c^\pm and IP_c^\pm . The two pairs of mutually orthogonal easy axes are rotated clockwise by $\sim 20^\circ$ from the z -axis within the y - z plane, in good agreement to the SQUID and NV-center measurements. As shown in Fig. 3b, the OP_c^\pm and IP_c^\pm states exhibit magnetization components of $m_z = \pm 0.94$ and ∓ 0.34 , respectively.

To elucidate the mechanism underlying the unusual four-state switching, we plot the simulated switching trajectories in Fig. 3c, d. The results reveal a distinct a two-step switching process. Taking the switching from OP_c^+ to IP_c^+ (Fig. 3c) as an example, the black arrow marks the initial stable state (\vec{m}_{init}). As previously described in Fig. 2e, upon current J excitation, \vec{m}_{init} begins to precess and flip under the influence of $\vec{\tau}_{\text{FL}}$ and $\vec{\tau}_{\text{DL}}$. However, it stabilizes at an intermediate stable state (\vec{m}_{mid}), whose direction is mainly determined by the balance between $\vec{\tau}_{\text{FL}}$ and $\vec{\tau}_{\text{Heff}}$ (torque induced by \vec{H}_{eff}). If J is below the threshold J_{c1} , \vec{m}_{mid} relaxes back to

\vec{m}_{init} once the pulse is removed (see the time evolution of m_x , m_y and m_z in Fig. 3e). But when $J \geq J_{c1}$, $\vec{\tau}_{\text{FL}}$ (green arrow in Fig. 3c) that exerts a $-\hat{z}$ direction torque, becomes strong enough to reduce the m_z component of \vec{m}_{mid} below a critical level. This is the key to the successful transition to IP_c^+ . After the pulse is turned off, $\vec{\tau}_{\text{Heff}}$ guides the moment toward the $-\hat{z}$ direction and settles it into the stable IP_c^+ state, i.e., \vec{m}_{final} . The corresponding time evolutions of m_x , m_y and m_z for $J = J_{c1}$ are shown in Fig. 3g, where the intermediate state remains metastable for most of the 20 ns pulse duration, except the initial ~ 2 ns transition period.

However, the mechanism underlying the IP_c^+ to OP_c^- transition differs markedly from the above case. As shown in Fig. 3d, the blue arrow represents the torque from the in-plane field \vec{H}_x ($\vec{\tau}_{\text{Hx}}$). In the above $\text{OP}_c^+ \rightarrow \text{IP}_c^+$ transition, $\vec{\tau}_{\text{Hx}}$ and $\vec{\tau}_{\text{Heff}}$ act in the same direction and thus are not separated. In contrast, for the $\text{IP}_c^+ \rightarrow \text{OP}_c^-$ transition, $\vec{\tau}_{\text{Hx}}$ is no longer aligned with $\vec{\tau}_{\text{Heff}}$, but instead opposes the z -component FL torque ($\vec{\tau}_{\text{FL},z}$). Specifically, $\vec{\tau}_{\text{FL},z}$ pushes the moment to the $+\hat{z}$ direction ($\vec{m}_{\text{init}} \times \vec{\sigma} \propto (-\hat{x}) \times (-\hat{y}) = \hat{z}$), whereas $\vec{\tau}_{\text{Hx}}$ acts oppositely ($-\vec{m}_{\text{init}} \times \vec{H}_x \propto -(+\hat{y}) \times (-\hat{x}) = -\hat{z}$). When $J > J_{c2}$, $\vec{\tau}_{\text{FL},z}$ dominates and displaces \vec{m}_{init} away from the OP_c^- anisotropy axis. Upon removing J , the IP_c^+ anisotropy prevails, causing \vec{m}_{mid} to relax back to \vec{m}_{init} (see the time revolution in Fig. 3f). As J is reduced from a large value to J_{c2} , $\vec{\tau}_{\text{Hx}}$ overcomes $\vec{\tau}_{\text{FL},z}$ and \vec{m}_{mid} moves closer to the OP_c^- anisotropy axis. Therefore, once J is turned off, $\vec{\tau}_{\text{Hx}}$ together with the OP_c^- anisotropy drives the system into the OP_c^- state (Fig. 3d). When J is further reduced, the magnetization remains trapped in the IP_c^+ state. Furthermore, as shown in Fig. S8, the switching trajectories and time-dependence for the $\text{OP}_c^- \rightarrow \text{IP}_c^-$ and $\text{IP}_c^- \rightarrow \text{OP}_c^+$ transitions are symmetric to those of $\text{OP}_c^+ \rightarrow \text{IP}_c^+$ and $\text{IP}_c^+ \rightarrow \text{OP}_c^-$, respectively, reflecting their shared underlying mechanisms.

Thus the numerical simulations successfully reproduce and explain the four-state switching loop. By combing the simulated energy landscape with the magnetization trajectories and their temporal evolution, we uncover the crucial role of multiple factors, particularly the four-fold anisotropy and the FL torque. More importantly, the switching mechanisms of $\text{OP}_c^\pm \rightarrow \text{IP}_c^\pm$ and $\text{IP}_c^\pm \rightarrow \text{OP}_c^\mp$ are different, accounting for their different dependences on H_x . For example, the $\text{OP}_c^+ \rightarrow \text{IP}_c^+$ transition is anisotropy-dominated, with $\vec{\tau}_{\text{Hx}}$ consistently assisting $\vec{\tau}_{\text{Heff}}$. Consequently, similar to conventional bistate SOT switching, J_{c1} decreases as H_x increases. In contrast, during the $\text{IP}_c^+ \rightarrow \text{OP}_c^-$ transition, H_x suppresses m_y , which contributes to a $-\hat{z}$ torque via $-\vec{m} \times \vec{H}_x = -(+\hat{y}) \times (-\hat{x}) = -\hat{z}$. As a result, a smaller FL

torque suffices to complete the switching, explaining why J_{C2} also decreases with increasing H_x . However, when H_x is further increased, $|m_x|$ exceeds $|m_y|$, enhancing the anisotropy torque associated with the IP_c^+ easy axis ($-\vec{m} \times (\vec{m} \times \vec{H}_{an}) = -\hat{z}$). This torque gradually overtakes $\vec{\tau}_{H_x}$ in competing with $\vec{\tau}_{FL,z}$, rendering J_{C2} less dependent on H_x . This trend agrees well with the experimental observation in Fig. 1d, where J_{C2} progressively saturates with increasing H_x .

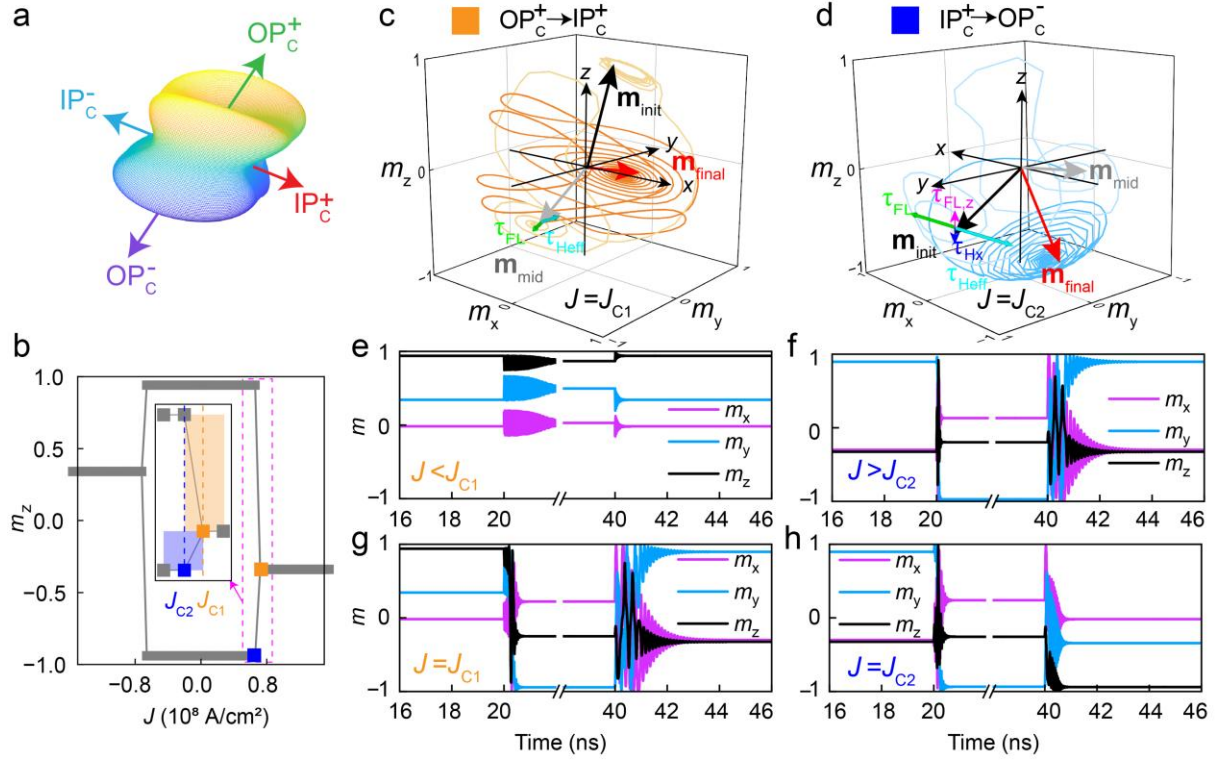


Figure 3. The spin dynamics simulations of the four-state switching loop. (a) The energy diagram of the system. (b) The m_z vs. J loop under $H_x = -300$ Oe and $\beta = 3$. The switching trajectory for (c) OP_c^+ to IP_c^+ , (d) IP_c^+ to OP_c^- . The black, gray and red arrows represent the \vec{m}_{init} , \vec{m}_{mid} , \vec{m}_{final} , respectively. The time evolution of (m_x, m_y, m_z) when (e) $J < J_{C1}$, (f) $J > J_{C2}$, (g) $J = J_{C1}$, and (h) $J = J_{C2}$.

Mapping Four-state Transitions, Stability and Programmable Writing/Reading

We thoroughly map all twelve transitions that a four-state device can maximally have. As shown in Fig. 4a, b, the four states are encoded as ‘0’ (OP_c^+), ‘1’ (IP_c^-), ‘2’ (IP_c^+) and ‘3’ (OP_c^-) to facilitate programming. The gray trajectories exhibit four transitions described previously, where the initial state is ‘0’. The newly explored trajectories are marked in red and blue, where the initial state is ‘2’ (Fig. 4a) or ‘1’ (Fig. 4b). In the red trajectory of Fig. 4a, after ‘writing’ the device into state ‘2’ with $J \geq J_{C1}$, J is turned off and then gradually increased from zero. The state ‘2’ switches to ‘3’ at $J = J_{C2}$, but ‘3’ reverts to ‘2’ when $J \geq J_{C1}$. Along the blue

trajectory (negative J), state ‘2’ is switched to ‘1’ when $J \leq -J_{c1}$. The latter two processes (‘3’ \rightarrow ‘2’, ‘2’ \rightarrow ‘1’) represent newly observed transitions. Similarly, in Fig. 4b, another two new transitions of ‘0’ \rightarrow ‘1’ and ‘1’ \rightarrow ‘2’ are revealed. All eight single-pulse transitions are summarized in Figure 4c, where orange and blue arrows indicate thresholds of $|J| \geq J_{c1}$ and $|J| = J_{c2}$, respectively. Solid and dash arrows denote positive and negative current. The remaining four transitions (‘0’ \rightarrow ‘3’, ‘2’ \rightarrow ‘0’, ‘3’ \rightarrow ‘0’, and ‘1’ \rightarrow ‘3’), all terminating in the OP_c^\pm states, require double-pulse excitation, making them particularly robust and suitable for fault-tolerant data writing.

The ‘0’ and ‘3’ states (OP_c^\pm) are clearly robust against small perturbations, such as current excitations below J_{c1} . We therefore turn to evaluate the stability of the previously unexplored ‘1’ and ‘2’ states (IP_c^\pm). As shown in the left panel of Fig. 4d, the device is initialized into state ‘2’ after completing the R_H vs. J loop with a final pulse of $J > J_{c1}$. Subsequently, R_H is continuously monitored using a low-amplitude AC current (Fig. 4d right panel). The measured R_H remains highly stable over an extended period of about three hours, exhibiting a standard deviation of $\pm 1.84\%$ over 2096 readings under a 300 Oe in-plane field, and $\pm 3.4\%$ over 2860 readings at zero field. These results verify the robustness of the IP_c^\pm states and demonstrates that all four states are stable against thermal perturbations or small energy excitations, confirming their suitability for non-volatile memory applications.

Finally, we demonstrate the programmable writing and reading of the four-state SOT device. Based on the established switching protocol, a positive pulse with $J \geq J_{c1}$ sets the device into state ‘2’ and a negative pulse with $J \leq -J_{c1}$ sets state ‘1’, both achievable from any initial state. To set the ‘3’ state from an arbitrary initial state, a double-pulse excitation sequence of ($J \geq J_{c1}$ and $J = J_{c2}$) is required. Similarly, a sequence of ($J \leq -J_{c1}$ and $J = -J_{c2}$) always set the state ‘0’. As shown in Fig. 4e, the programmed writing follows the sequence ‘2’ \rightarrow ‘1’, ‘3’ \rightarrow ‘0’ \rightarrow ... \rightarrow ‘3’ \rightarrow ‘1’, each followed by 50 consecutive readings over a period of 250 s. Indeed, each target state is accurately written and stably maintained throughout the entire reading period. The repeatability of writing is also verified, e.g. at $t = 1100$ s, the 2nd pair of ($J \leq -J_{c1}$, $J = -J_{c2}$) pulses reproducibly resets the ‘0’ state.

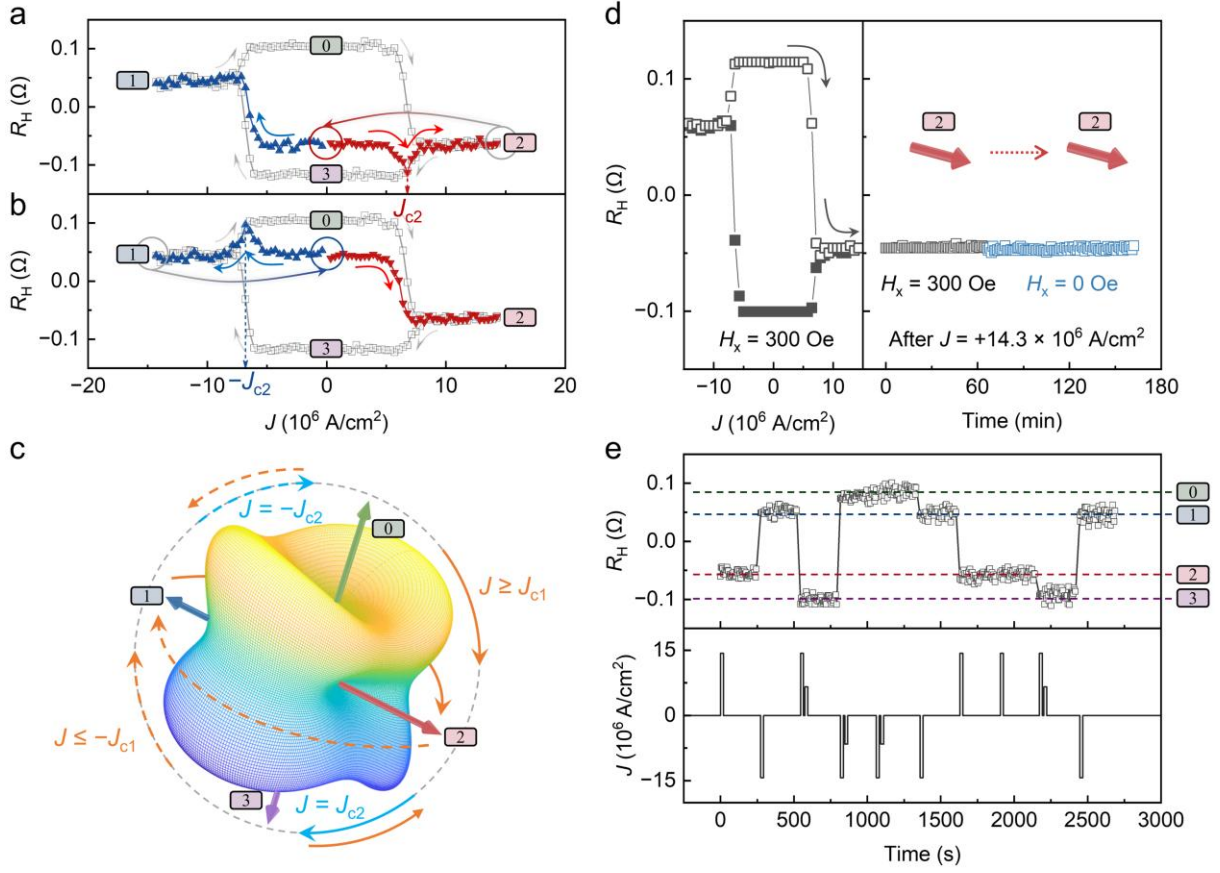


Figure 4. Mapping transition paths, stability verification and programmable writing/reading. (a) The blue and red trajectories represent transition paths starting from state ‘2’ (IP_C^+) state, and (b) from state ‘1’ (IP_C^-), both under $H_x = +300$ Oe at 60 K. The gray color trajectory represents the loop starting from state ‘0’, which has been discussed in Fig. 1-3. (c) Schematic illustrations of the eight single-pulse switching paths. The orange and blue arrows represent $J \geq J_{c1}$ and $J = J_{c2}$, respectively. Solid (dashed) arrows indicate positive (negative) J . (d) Temporal stability of the ‘2’ (IP_C^+) state after being prepared by $J > J_{c1}$. (e) Programmed writing and reading of the four-state SOT device.

CONCLUSIONS

We investigate the performance and switching mechanism of an intrinsic multistate SOT device hosting four stable yet electrically distinguishable spin-canted states, IP_C^\pm and OP_C^\pm . Among these states, eight distinct transitions are driven by single-pulse current excitations and four by double-pulse excitations, all governed by two critical current densities that define the complete four-state switching protocol. NV-center magnetometry and spin dynamics simulations reveal that the effective anisotropy field H_{eff} of the four-canted configuration plays a pivotal role, acting in concert with spin torques to direct each switching pathway. The intrinsic four-state SOT device achieves deterministic, repeatable, and nonvolatile read/write

operations, opening a new paradigm for compact, high-density SOT technology. The design principle revealed here is broadly applicable to multiaxial spin-canted ferromagnets across diverse material families.

METHODS

Sample growth and device fabrication

The SRO (6 nm) and SIO (8 nm) bilayer film was epitaxially grown on a $5 \times 5 \text{ nm}^2$ TiO₂-terminated SrTiO₃ (0 0 1) substrate employing in-situ reflection high-energy electron diffraction (RHEED) assisted pulsed laser deposition (PLD). During deposition, the substrate temperature was 625 °C and the oxygen pressure was 10 Pa. The laser energy fluence was 1.35 J/cm² and 1.25 J/cm² for depositing SRO and SIO, respectively. After deposition, samples were cooled down to room temperature at a rate of 20 °C/min under the same oxygen pressure of 10 Pa. Hall bar patterns with a channel width of 10 μm were transferred to the bilayer films using laser writing and Ar ion milling. Finally, the Ti (10 nm)/Au (60 nm) electrodes were deposited utilizing a magnetron sputtering system.

Electrical transport and magnetization measurements

The magneto-transport measurements were performed in a He₄ refrigerator (Oxford Teslatron PT system). For current-induced switching measurements, the current pulse sequences were custom-programmed, and each d.c. pulse was sequentially generated by a Keithley 6221 and applied to the current path of the Hall bar. Each current pulse was precisely set to 30 μs by configuring the current source in square-wave mode with a specific duty cycle. After each pulse and a sufficiently long cooling time (10 s), a small a.c. excitation (10 μA) was applied to measure the R_H . The a.c. voltage measurements were performed using Stanford Research Systems SR830. The SOT current pulse excitation and measurement sequences are illustrated in Fig. S4. The magnetic properties were measured using a Quantum Design Magnetic Properties Measurement System.

Scanning NV-center microscopy set-up and measurement principle

All NV-based magnetometry measurements were performed using a custom-built ultra-high-vacuum, NV-center scanning microscope developed in collaboration with CIQTEK. The system operates over a temperature range of 4-300 K and is equipped with a three-axis vector magnet providing fields of 300, 300 and 1500 Oe along the x , y , and z directions, respectively.

During the NV measurements, the sample was polarized by current pulses from -20 mA to +20 mA, following the switching loop and under an in-plane field of 300 Oe. After the current-pulse switching, the 300 Oe magnetic field was removed while a $B_{\text{bias}} = 20$ Oe field was applied along the NV axis during the magnetic imaging. We measured the magnetic field above

the sample based on optically detected magnetic resonance (ODMR). The negatively charged NV center exhibits a spin-triplet ground state. With an external magnetic field B_{\parallel} applied along the NV axis, the spin states $|m_s = \pm 1\rangle$ exhibit Zeeman splitting of $f_{\pm 1} = D_s \pm \gamma_e B_{\parallel}$ from $|m_s = 0\rangle$, where $D_s = 2.87$ GHz is the zero field splitting, and $\gamma_e = 28$ GHzT⁻¹ is the electronic spin gyromagnetic ratio. By sweeping the microwave frequency and monitoring the fluorescence, both frequency f_{+1} and f_{-1} are tracked and the B_{\parallel} above the sample can be determined by $B_{\parallel} = \frac{|f_{+1} - f_{-1}|}{2\gamma_e} - B_{\text{bias}}$.

Spin dynamics simulations

The magnetization dynamics were simulated by solving the LLG equation with SOT terms. The magnetic anisotropy energies were set as $K_u = 3.25 \times 10^5$ J/m³, $K_y = 1.625 \times 10^5$ J/m³, and $K_x = 0.975 \times 10^5$ J/m³, corresponding to the uniaxial anisotropy constants along the z , y , and x axes, respectively. These values are chosen to reflect the magnetization preference along the x -, y -, z -axis in the experimental magnetization data in Fig. S3. In addition, a fourfold anisotropy term $K_{4u} = 0.975 \times 10^5$ J/m³ was included [32]. $B_D = \frac{\hbar J_c \theta_{\text{SH}}}{2 M_s t}$ and B_F represent the magnitude of DL and FL torques, respectively, where $\theta_{\text{SH}} = 0.5$ is the spin-Hall angle of SIO. M_s and t are the saturation magnetization and the FM layer thickness, in agree with the experimental values.

SUPPLEMENTARY DATA

Supplementary data are available at NSR online.

ACKNOWLEDGMENTS

We thank Prof. Kaiyou Wang and Prof. Xuepeng Qiu for valuable discussions.

FUNDING

This work was supported by the National Key Research and Development Program of China (Grant No. 2023YFA1406301, 2022YFA1403000), the National Natural Science Foundation of China (Grant No. 62574134), the Natural Science Foundation of Shanghai (Grant No. 25ZR1402375), and the China Postdoctoral Science Foundation (Grant No. KLH1512149). The simulation conducted in this work is supported by HPC Platform and SIST Computing Platform at ShanghaiTech University. The research used resources from Analytical Instrumentation Center (#SPST-AIC10112914) and Soft Matter Nanofab (SMN180827) in

ShanghaiTech University. XF.Z. and Z.Z. acknowledge start-up grants of ShanghaiTech University.

AUTHOR CONTRIBUTIONS

XF.Z., Z.W., and Z.Z. conceived the idea. C.G. and XF. Z. supervised the project. XF.Z. and Z.W. designed the experiments. F.Y. fabricated samples, performed the electric transport and magnetization measurements with help from L.C.. C.W., S.J., and Z.W. performed the NV-center experiments. X.Z. and Z.Z. performed the spin dynamics simulations. All authors discussed the results in the paper. Z.W., F.Y., X.Z., and C.W. wrote the initial paper, which was revised by XF.Z., Z.Z. and C.G., and approved by all authors.

Conflict of interest statement. None declared.

REFERENCES

1. Liu L, Lee OJ and Gudmundsen TJ *et al.* Current-induced switching of perpendicularly magnetized magnetic layers using spin torque from the spin Hall effect. *Phys. Rev. Lett.* 2012; **109**: 096602.
2. Pai CF, Liu L and Li Y *et al.* Spin transfer torque devices utilizing the giant spin Hall effect of tungsten. *Appl. Phys. Lett.* 2012; **101**: 122404.
3. Sinova J, Valenzuela SO and Wunderlich J *et al.* Spin Hall effects. *Rev. Mod. Phys.* 2015; **87**: 1213–1260.
4. Gilbert TL. A phenomenological theory of damping in ferromagnetic materials. *IEEE Trans. Magn.* 2004; **40**: 3443–3449.
5. Yu G, Upadhyaya P and Fan Y *et al.* Switching of perpendicular magnetization by spin–orbit torques in the absence of external magnetic fields. *Nat. Nanotechnol.* 2014; **9**: 548–554.
6. Fukami S, Zhang C and DuttaGupta S *et al.* Magnetization switching by Spin–Orbit torque in an antiferromagnet–ferromagnet bilayer system. *Nat. Mater.* 2016; **15**: 535–541.
7. Liu L, Qin Q and Lin W *et al.* Current-induced magnetization switching in all-oxide heterostructures. *Nat. Nanotechnol.* 2019; **14**: 939–944.
8. Yang Q, Han D and Zhao S *et al.* Field-free spin–orbit torque switching in ferromagnetic trilayers at sub-ns timescales. *Nat. Commun.* 2024; **15**: 1814.
9. Fan Y, Upadhyaya P and Kou X *et al.* Magnetization switching through giant spin–orbit torque in a magnetically doped topological insulator heterostructure. *Nat. Mater.* 2014;

- 13:** 699–704.
10. Wang Y, Ramaswamy R and Motapothula M *et al.* Room-temperature giant charge-to-spin conversion at the SrTiO₃–LaAlO₃ oxide interface. *Nano Lett.* 2017; **17**: 7659–7664.
 11. Cao Y, Rushforth AW and Sheng Y *et al.* Tuning a binary ferromagnet into a multistate synapse with spin–orbit-torque-induced plasticity. *Adv. Funct. Mater.* 2019; **29**: 1808104.
 12. Fan Y, Han X and Zhao X *et al.* Programmable spin–orbit torque multistate memory and spin logic cell. *ACS Nano* 2022; **16**: 6878–6885.
 13. Sheng Y, Li YC and Ma XQ *et al.* Current-induced four-State magnetization switching by spin–orbit torques in perpendicular ferromagnetic trilayers. *Appl. Phys. Lett.* 2018; **113**: 112406.
 14. Klein L, Dodge JS and Geballe TH *et al.* Perpendicular magnetic anisotropy and strong magneto-optic properties of SrRuO₃ epitaxial films. *Appl. Phys. Lett.* 1995; **66**: 2427–2429.
 15. Koster G, Klein L and Siemons W *et al.* Structure, Physical properties, and applications of SrRuO₃ thin films. *Rev. Mod. Phys.* 2012; **84**: 253–298.
 16. Cui Z, Grutter AJ and Zhou H *et al.* Correlation-driven eightfold magnetic anisotropy in a two-dimensional oxide monolayer. *Sci. Adv.* 2020; **6**: eaba0114.
 17. Nan T, Anderson TJ and Gibbons J *et al.* Anisotropic spin–orbit torque generation in epitaxial SrIrO₃ by symmetry design. *Proc. Natl. Acad. Sci. U.S.A.* 2019; **116**: 16186–16191.
 18. Zheng D, Lan J and Fang B *et al.* High-efficiency magnon-mediated magnetization switching in all-oxide heterostructures with perpendicular magnetic anisotropy. *Adv. Mater.* 2022; **34**: 2203038.
 19. Zhu L, Ralph DC and Buhrman RA. Lack of simple correlation between switching current density and spin–orbit-torque efficiency of perpendicularly magnetized spin-current-generator–ferromagnet heterostructures. *Phys. Rev. Appl.* 2021; **15**: 024059.
 20. Miron IM, Garello K and Gaudin G *et al.* Perpendicular switching of a single ferromagnetic layer induced by in-plane current injection. *Nature* 2011; **476**: 189–193.
 21. Liu L, Pai CF and Li Y *et al.* Spin-torque switching with the giant spin Hall effect of tantalum. *Science* 2012; **336**: 555–558.
 22. Meng K, Miao J and Xu X *et al.* Modulated switching current density and spin–orbit torques in MnGa/Ta films with inserting ferromagnetic layers. *Sci. Rep.* 2016; **6**: 38375.
 23. Han J, Richardella A and Siddiqui SA *et al.* Room-temperature spin–orbit torque switching induced by a topological insulator. *Phys. Rev. Lett.* 2017; **119**: 077702.

24. Wang Y, Zhu D and Wu Y *et al.* Room-temperature magnetization switching in topological insulator–ferromagnet heterostructures by spin–orbit torques. *Nat. Commun.* 2017; **8**: 1364.
25. Khang NHD, Ueda Y and Hai PN. A conductive topological insulator with large spin Hall effect for ultralow power spin–orbit torque switching. *Nat. Mater.* 2018; **17**: 808–813.
26. Alghamdi M, Lohmann M and Li J *et al.* Highly efficient spin–orbit torque and switching of layered ferromagnet Fe₃GeTe₂. *Nano Lett.* 2019; **19**: 4400–4405.
27. Lee H-Y, Kim S and Park J-Y *et al.* Enhanced spin–orbit torque via interface engineering in Pt/CoFeB/MgO heterostructures. *APL Mater.* 2019; **7**: 031110.
28. Li X, Li P and Hou VD-H *et al.* Large and robust charge-to-spin conversion in sputtered conductive WTe_x with disorder. *Matter* 2021; **4**: 1639–1653.
29. Shin I, Cho WJ and An E-S *et al.* Spin–orbit Torque switching in an all–Van der Waals heterostructure. *Adv. Mater.* 2022; **34**: 2101730.
30. Dou P, Zhang J and Zhu T *et al.* High Spin–orbit torque efficiency induced by engineering spin absorption for fully electric-driven magnetization switching. *Mater. Horiz.* 2025; **12**: 2554–2563.
31. Zhang X, Xu Z and Zhu Z. Revisiting the analytical solution of spin–orbit torque–switched nanoscale perpendicular ferromagnets. *Phys. Rev. B* 2024; **110**: 184428.
32. Zhang P, Das A and Barts E *et al.* Robust skyrmion-bubble textures in SrRuO₃ thin films stabilized by magnetic anisotropy. *Phys. Rev. Res.* 2020; **2**: 032026